

Learnable Burst-Encodable Time-of-Flight Imaging for High-Fidelity Long-Distance Depth Sensing

Manchao Bao¹

manchaobao@smail.nju.edu.cn

Shengjiang Fang¹

shengjiangfang@smail.nju.edu.cn

Tao Yue¹

yuetao@nju.edu.cn

Xuemei Hu¹

xuemeihu@nju.edu.cn

¹Nanjing University

Abstract

Long-distance depth imaging holds great promise for applications such as autonomous driving and robotics. Direct time-of-flight (dToF) imaging offers high-precision, long-distance depth sensing, yet demands ultra-short pulse light sources and high-resolution time-to-digital converters. In contrast, indirect time-of-flight (iToF) imaging often suffers from phase wrapping and low signal-to-noise ratio (SNR) as the sensing distance increases. In this paper, we introduce a novel ToF imaging paradigm, termed Burst-Encodable Time-of-Flight (BE-ToF), which facilitates high-fidelity, long-distance depth imaging. Specifically, the BE-ToF system emits light pulses in burst mode and estimates the phase delay of the reflected signal over the entire burst period, thereby effectively avoiding the phase wrapping inherent to conventional iToF systems. Moreover, to address the low SNR caused by light attenuation over increasing distances, we propose an end-to-end learnable framework that jointly optimizes the coding functions and the depth reconstruction network. A specialized double well function and first-order difference term are incorporated into the framework to ensure the hardware implementability of the coding functions. The proposed approach is rigorously validated through comprehensive simulations and real-world prototype experiments, demonstrating its effectiveness and practical applicability.

1 Introduction

Achieving high-precision depth imaging over long distances has remained a fundamental objective in fields such as computer vision, robotics, and autonomous systems. Time-of-flight (ToF) imaging [1, 2, 3], as a key approach to depth imaging, can be further categorized into direct ToF (dToF) and indirect ToF (iToF) based on differences in working principles. Direct ToF imaging [4] estimates depth by directly measuring the round-trip time of light, enabling high-precision and long-range sensing. Despite its advantages, this approach requires ultra-short pulsed light sources and high-resolution time-to-digital converters (TDCs), imposing stringent hardware demands that increase system complexity and cost, thereby limiting its practicality for widespread deployment. Indirect ToF systems [5, 6, 7, 8], in contrast, emit amplitude-modulated continuous wave (AMCW) signals and infer depth by analyzing the phase shift between the transmitted and received signals. Due to their relatively lower hardware complexity and cost, iToF systems offer a more practical and hardware-friendly solution. Nevertheless, existing iToF technologies face significant challenges in long-range imaging, primarily due to phase wrapping [9] and low signal-to-noise ratio (SNR) resulting from optical attenuation [10]. To address the phase wrapping, dual-frequency modulation

techniques [11, 12] have been proposed, albeit at the cost of increased computational complexity and stricter hardware synchronization requirements. Alternative approaches have sought to mitigate phase wrapping under single-frequency modulation by incorporating scene priors [5, 13], however, these methods do not fundamentally resolve the intrinsic ambiguity introduced by periodic modulation.

In this paper, we propose a novel ToF imaging paradigm termed Burst-Encodable Time-of-Flight (BE-ToF). Our BE-ToF system employs a low-frequency burst mode to modulate and demodulate high-frequency light pulses, wherein the phase shift of the reflected signal spans the full range $[0, 2\pi]$ within a single burst period. This facilitates high-fidelity, long-distance depth imaging using only single frequency modulation. Moreover, considering the significant variation in SNRs caused by the light-falloff, we propose an end-to-end learnable framework that jointly optimizes the coding functions and the depth reconstruction network, thereby ensuring high-precision depth estimation. In particular, we incorporate constraints based on double well function and first-order difference to ensure the hardware implementability of the learned coding functions. We evaluate our method on a synthetic dataset and compare it with conventional iToF approaches, including single-frequency and multi-frequency modulation techniques. Finally, we built a prototype system to prove the effectiveness of our method in real-world experiments.

In general, we make the following contributions:

- We present a novel Burst-Encodable Time-of-Flight imaging system that enables high-fidelity long-distance depth sensing using only a single modulation frequency, thereby fundamentally mitigating the issue of phase wrapping inherent in traditional iToF systems.
- We propose an end-to-end learnable framework that jointly optimizes the coding functions and the depth reconstruction network to ensure high-precision depth estimation across varying distances.
- We uniquely incorporate double well function and first-order difference as loss function to ensure the hardware implementability of the learnable coding functions.
- We develop a prototype of our BE-ToF system and demonstrate its superior performance on both simulated datasets and real-world scenarios.

2 Related Work

ToF imaging. ToF imaging has emerged as a prevalent and effective technique for depth acquisition. Direct ToF imaging enables long-range depth estimation by measuring the round-trip time of light pulses [14]. However, achieving high-precision depth measurements with dToF imposes stringent requirements on the pulsed light source, typically necessitating pulse widths in the nanosecond or picosecond range [4, 15, 16]. In addition, the system requires high-resolution TDCs with picosecond-level timing precision [17, 18]. These demanding hardware specifications present substantial challenges for practical implementation and large-scale deployment. In contrast, indirect ToF imaging leverages cost-effective CMOS sensors to deliver high-resolution depth estimation. However, iToF often faces phase ambiguity caused by phase wrapping when performing long-range depth imaging. A viable approach to address this issue is the use of multi-frequency modulation [11, 19], where low frequencies are employed to extend the maximum unambiguous range, while high frequencies ensure precise depth measurements. Hanto *et al.* [20] developed a novel ToF LiDAR range finder based on dual-modulation frequency switching to achieve depth imaging with an extended range. Su *et al.* [21] propose an end-to-end time-of-flight imaging framework that enables high-quality depth reconstruction under multi-frequency modulation. However, multi-frequency modulation often results in increased hardware complexity and computational cost. In addition, various approaches such as amplitude correction [5] and surface normal constraints [13] have been proposed to enable phase unwrapping from single-frequency measurements, which extremely rely on the scene prior. In this paper, we propose Burst-Encodable Time-of-Flight Imaging to fundamentally solve the phase wrapping issue in iToF, enabling high-fidelity, long-distance depth estimation.

End-to-end learning. End-to-end learning is a method aimed at jointly optimizing optical systems and reconstruction algorithms. Metzler *et al.* [22, 23] obtain high dynamic range (HDR) images from a single shot by jointly optimizing the optical encoder and the electronic decoder. Nie *et al.* [24] leverage an end-to-end network for hyperspectral reconstruction, enabling simultaneous learning of optimized camera spectral response functions and a mapping for spectral reconstruction. For

dense 3D localization microscopy, Nehme *et al.* [25] proposed a deep STORM-based method to achieve end-to-end optimization of point spread function engineering and accurate 3D localization. To extend the depth of field (EDOF), Sitzmann *et al.* [26] proposed jointly optimizing the optical system and the reconstruction algorithm’s parameters to achieve achromatic EDOF imaging. Guo *et al.* [27] put forward an end-to-end network framework capable of jointly optimizing the encoding function and exposure time to improve the accuracy of fluorescence lifetime imaging. Besides, in iToF imaging, Chugunov *et al.* [28] proposed to jointly learn a microlens amplitude mask and an encoder-decoder network to reduce flying pixels in depth captures. Li *et al.* [10] put forward a Fisher-information guided framework for the joint optimization of the coding functions and the reconstruction network. Given the remarkable potential of end-to-end learning in elevating imaging performance, we propose an end-to-end learnable framework that jointly optimizes the coding functions and depth reconstruction network of our BE-ToF, ensuring high-quality depth performance across varying distances.

3 Learnable Burst-Encodable Time-of-Flight Imaging

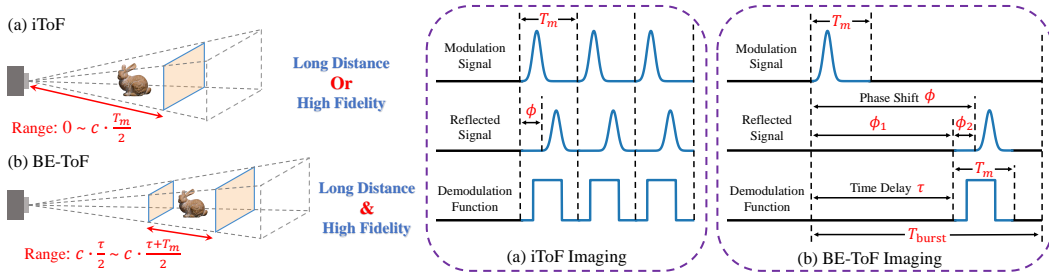


Figure 1: Comparison between iToF and BE-ToF. (a) Principle of iToF imaging, which suffers from a trade-off between sensing distance and precision; (b) Principle of BE-ToF imaging, enabling long-distance and high-fidelity depth sensing through modulation and demodulation in burst mode.

In this section, we first introduce the working principle of our BE-ToF. The core idea of our BE-ToF is to modulate and demodulate high-frequency light pulses using a low-frequency burst mode. As illustrated in Fig. 1(b), within a single long burst period T_{burst} , a short-cycle T_m light pulse is emitted. When the reflected signal returns with a phase shift ϕ , it can be demodulated by coding functions with controllable time delay. Specifically, the total phase shift ϕ can be decomposed into two components: ϕ_1 , which is primarily determined by the time delay τ , and ϕ_2 , which can be recovered using demodulation techniques like 4-step phase shift or deep learning. In summary, the depth d can be defined as Eq. 1

$$d = \frac{c(\phi_1 + \phi_2)T_{burst}}{4\pi} = \frac{c\tau}{2} + \mathcal{D}(\phi_2) \quad (1)$$

where c is the light speed and $\mathcal{D}(\phi_2)$ represents the demodulation process of ϕ_2 .

Thus, in our BE-ToF system, the maximum unambiguous range d_{mur} is decided by T_{burst} , following $d_{mur} = \frac{c \cdot T_{burst}}{2}$, while depth accuracy ϵ_d is governed by T_m as $\epsilon_d = \frac{c \cdot \epsilon_\phi \cdot T_m}{4\pi}$, where ϵ_ϕ is the phase error during the demodulation process. Consequently, our BE-ToF system is capable of achieving both long-distance and high-precision depth imaging simultaneously. Furthermore, the depth sensing range in a single measurement spans from $\frac{c \cdot \tau}{2}$ to $\frac{c \cdot (\tau + T_m)}{2}$, which can be flexibly adjusted by tuning the time delay τ .

3.1 Differential BE-ToF Imaging Model

As described above, given the operating principle of BE-ToF, it can be readily implemented using a pulsed laser and an encodable exposure camera [29]. Based on this, we first establish the differentiable physical model of our BE-ToF for end-to-end optimization. Assuming $M(t)$ is the modulation signal emitted by pulse laser, the reflected signal of scene point $s \in \mathbb{R}^3$ can be defined as Eq. 2

$$R(s, t) = \rho_s M(t - 2\frac{d(s)}{c}) + I_{amb} \quad (2)$$

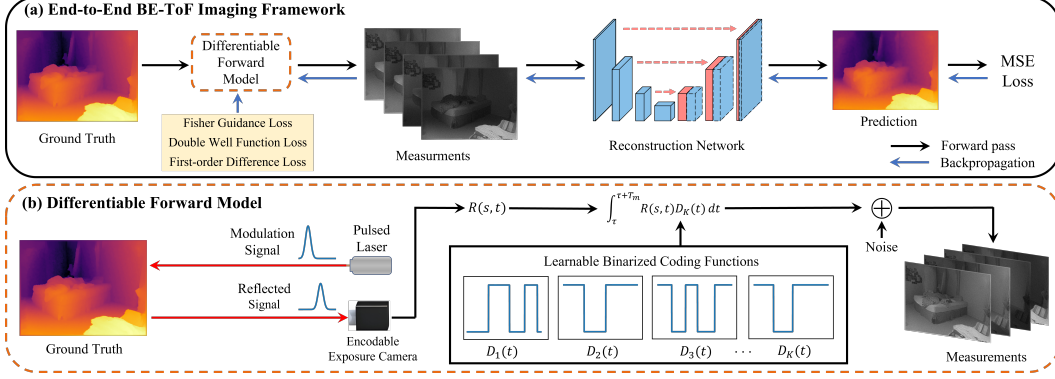


Figure 2: (a) End-to-end BE-ToF imaging framework for jointly optimizing the demodulation function and reconstruction network, (b) The differentiable physical model of the BE-ToF system.

where ρ_s is the inherent reflectance of the scene point s , I_{amb} is the interference caused by ambient light, $d(s)$ denotes the depth value of point s . Furthermore, considering the attenuation of light intensity with distance during propagation, we incorporate the attenuation function into our model as Eq. 3

$$R(s, t) = \mathcal{F}_{d(s)} \rho_s M(t - 2\frac{d(s)}{c}) + I_{amb} \quad (3)$$

where $\mathcal{F}_{d(s)}$ is the attenuation coefficient of the emitted light $M(t)$ at depth $d(s)$, which is typically inversely proportional to the square of the distance [30]. Finally, the whole BE-ToF imaging process can be formulated as Eq. 4

$$I_i(s) = \int_{\tau}^{\tau+T_m} R(s, t) D_i(t) dt, \quad i \in 1, \dots, K \quad (4)$$

where $I_i(s)$ is the measurement value of the camera, $D_i(t)$ denotes the coding functions and K denotes the number of measurements. Taking into account the inherent noise of the sensor, the final measurement can be expressed as Eq. 5

$$X_i(s) = I_i(s) + n_d + n_r, \quad n_d \sim \mathcal{P}(\mathbb{E}(n_d)), \quad n_r \sim \mathcal{N}(0, \sigma_r^2) \quad (5)$$

where n_d is the dark noise following the poisson distribution with expectation $\mathbb{E}(n_d)$ and n_r is the readout noise following gaussian distribution with standard deviation σ_r .

Considering that $X_i(s)$ contains three unknowns: ρ_s , I_{amb} , $\mathcal{F}_{d(s)}$. Therefore, at least $K \geq 3$ measurements are required to solve for the depth $d(s)$.

3.2 Reconstruction Network

With the proposed differentiable forward model, we can simulate the K measurements of the BE-ToF imaging process. To recover high-fidelity depth map from this set of measurements, we propose a Restormer-based Spatial-Channel Fusion Network(RSCF-Net). As shown in Fig. 3, our network adopts Restormer [31] as the backbone, featuring a four-level encoder-decoder structure in which each level comprises multiple Restormer blocks. In contrast to the conventional skip connections used in the original Restormer, we integrate an Efficient Channel Attention (ECA) module [32] to enhance the fusion of features between encoder and decoder branches. Furthermore, recognizing the inherent differences between depth reconstruction and the image restoration tasks for which Restormer was originally designed, we augment our network with two additional components: the Channel Feature Extraction Block (CFEB) and the Multi-scale Feature Fusion Block (MFFB). The CFEB is composed of multiple residual-connected 1×1 convolutional layers, designed to extract inter-channel relationships across multiple per-pixel measurements. On the other hand, the MFFB emphasizes spatial structure by performing preliminary depth estimation at each decoder level and progressively integrating features from multiple scales in a coarse-to-fine manner. The outputs of CFEB and MFFB are subsequently fused to produce the final high-fidelity depth map.

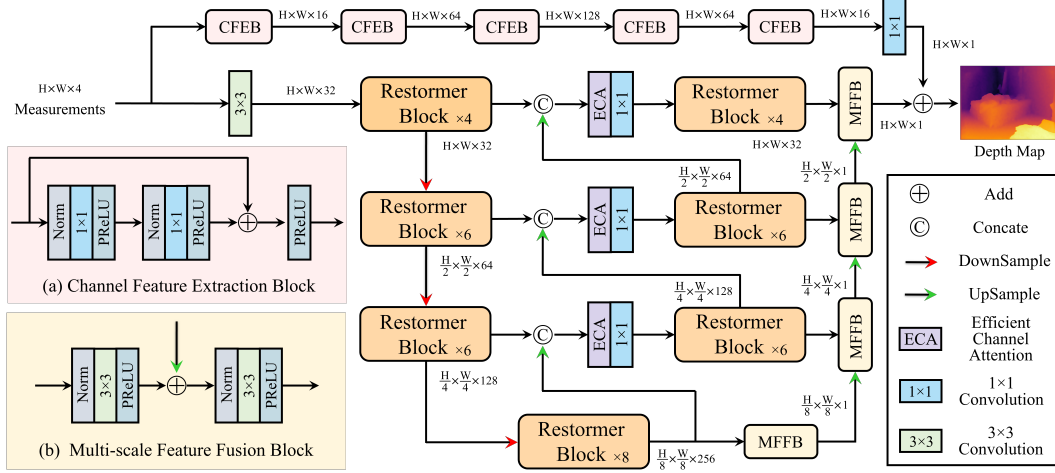


Figure 3: Architecture of the Restormer-based Spatial-Channel Fusion Network(RSCF-Net), (a) Channel Feature Extraction Block(CFEB), (b) Multi-scale Feature Fusion Block(MFFB).

3.3 Loss Function

During the training process, we jointly optimize the coding functions and the reconstruction network. Given that our encodable exposure camera supports only binarized coding functions, we enforce hardware implementability by applying constraints based on a double well function and first-order difference. Additionally, Fisher information is incorporated into the loss to improve reconstruction quality, while mean squared error (MSE) is used as the objective to guide the final output. Here we give more details about these losses.

Double Well Function Loss. To enable the optimization of binarized coding functions within the differentiable physical model. We introduce the double well function from quantum mechanics [33], which is formulated in Eq. 6

$$f_{dw}(x) = 4(x - 0.5)^4 - 2(x - 0.5)^2 \quad (6)$$

As shown in Fig. 4, this function has two valleys at $x = 0$ and $x = 1$, thereby encouraging the coding functions to converge toward binary states during the optimization process. Therefore, our double well function loss can be defined as Eq. 7

$$\mathcal{L}_{dw} = \sum_{i=1}^K \sum_{j=1}^M f_{dw}(D_i(t_j)) \quad (7)$$

where M is the sampling points on each coding function.

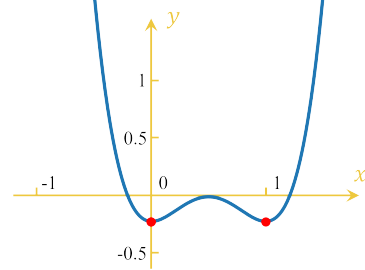


Figure 4: Demonstration of the double well function with two identical minima located at $x = 0$ and $x = 1$.

First-order Difference Loss. Although the double well function effectively constrains the coding functions to a binary state, we observe that the learned functions often exhibit extremely narrow peaks, which pose challenges for practical hardware implementation. To mitigate this issue, we introduce a first-order difference loss, as defined in Eq. 8. By minimizing the first-order difference loss, narrow peaks can be effectively suppressed, thus ensuring feasibility for hardware implementation.

$$\mathcal{L}_{1st} = \sum_{i=1}^K \sum_{j=1}^{M-1} |D_i(t_{j+1}) - D_i(t_j)| \quad (8)$$

Fisher Guidance Loss. The SNR is one of the key factors influencing the quality of ToF imaging. Inspired by [10], we introduce the fisher guidance loss to enhance the quality of our depth reconstruction, which can be summarized as Eq. 9

$$\mathcal{L}_{fisher} = - \sum_s \sum_{i=1}^K \left[\frac{1}{2\sigma_i^4(s)} + \frac{1}{\sigma_i^2(s)} \right] \left[\frac{\partial \mathbb{E}(I_i(s))}{\partial d} \right]^2 \quad (9)$$

where $\mathbb{E}(I_i(s))$ is the expectation of $I_i(s)$ and $\sigma_i(s) = \sqrt{\mathbb{E}(I_i(s)) + \mathbb{E}(n_d) + \sigma_r^2}$.

Mean Squared Error Loss. We employ MSE as the fidelity loss to supervise the predicted depth map, as defined in Eq. 10

$$\mathcal{L}_{MSE} = \sum_s \|d_{pre}(s) - d_{gt}(s)\|_2^2 \quad (10)$$

Finally, our complete loss can be summarized as Eq. 11

$$\mathcal{L} = \mathcal{L}_{MSE} + \gamma_1 \mathcal{L}_{fisher} + \gamma_2 \mathcal{L}_{dw} + \gamma_3 \mathcal{L}_{1st} \quad (11)$$

where γ_1 , γ_2 and γ_3 are loss balance coefficients.

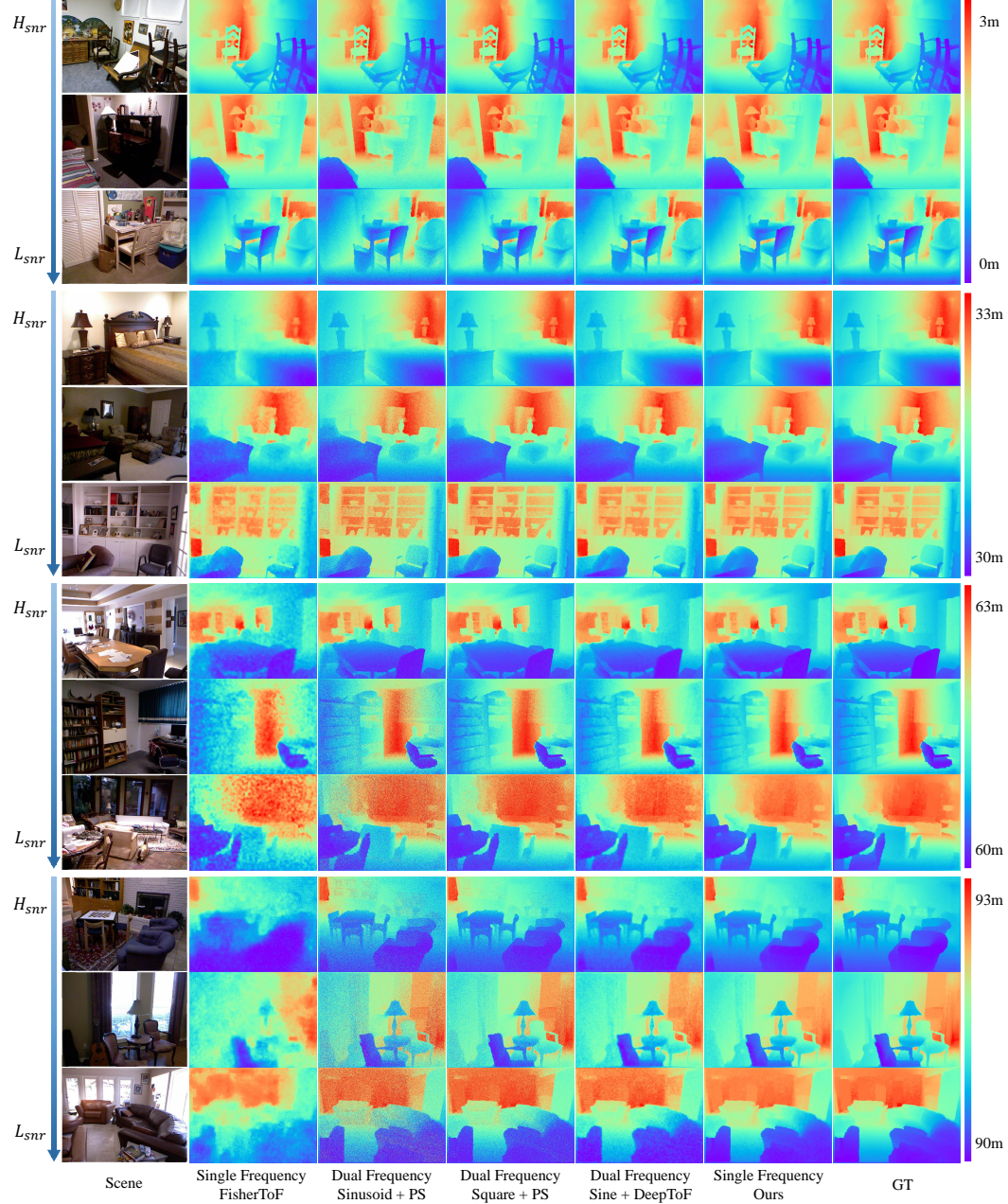


Figure 5: Overall comparisons with traditional iToF methods under various distances and SNRs, including FisherToF [10] under single frequency modulation; Sine/Square + PS algorithm [5] and Sine + DeepToF [21] under dual frequency modulation.

Table 1: Quantitative comparison of overall performance, coding schemes, and reconstruction networks. All metrics are reported as MAE (mm).

	0-3m			30-33m			60-63m			90-93m		
	H_{snr}	M_{snr}	L_{snr}	H_{snr}	M_{snr}	L_{snr}	H_{snr}	M_{snr}	L_{snr}	H_{snr}	M_{snr}	L_{snr}
(a) Overall Performance												
Sine+PS [5]	43.26	58.08	78.09	56.96	77.89	107.25	79.20	111.49	158.40	117.21	170.76	244.29
Square+PS [5]	33.21	40.64	51.29	40.06	51.19	66.90	51.90	69.12	93.62	72.16	100.12	140.98
DeepToF [21]	17.76	19.19	29.51	26.54	29.25	37.49	31.50	35.02	45.54	42.64	45.12	56.97
FisherToF [10]	7.19	10.46	16.91	20.80	24.54	31.61	34.58	42.43	54.73	75.19	77.68	138.11
(b) Coding Scheme												
Square	12.66	15.18	21.35	16.82	22.10	29.05	20.85	24.54	32.77	25.51	30.08	44.47
(c) Reconstruction Network												
DeepToF [21]	14.76	16.20	20.32	18.25	23.30	34.12	24.95	31.50	37.90	28.12	38.17	48.55
MaskToF [28]	11.73	12.89	17.41	14.72	19.44	26.73	15.94	21.38	33.55	25.71	27.86	38.60
FisherToF [10]	6.94	8.10	16.26	10.22	15.71	21.68	14.62	18.31	29.73	22.60	24.89	31.83
Ours	5.90	6.95	12.71	8.03	12.25	18.29	11.93	16.60	26.08	18.96	21.99	29.58

4 Synthetic Assessment

4.1 Implementation Details

Dataset. We use the NYU-V2 dataset [34] to train and test our end-to-end framework. The NYU-V2 dataset is a high-quality RGB-D dataset captured by Kinect with a resolution of 640×480 . It contains a total of 1449 pairs of precisely aligned RGB and depth images collected from 464 indoor scenes, which enables its extensive application in academic research. For each RGB-D pair, we initially employ intrinsic image decomposition [35] to break down the RGB image into albedo map and shading map. Subsequently, we designate the R-channel of the albedo map as the albedo component ρ_s mentioned in Eq. 2, and the average of the three RGB channels of the albedo map is taken as the ambient component I_{amb} in the same equation. We divide the dataset in detail, using 1000 pairs of data as the training set and the remaining 449 pairs as the test set [36, 37].

Incremental Training Method. In our BE-ToF system, the SNR varies not only with distance but also significantly under the same distance due to ambient light I_{amb} . Therefore, we introduce an incremental training strategy [38] to ensure robust depth estimation of our network under varying SNR levels. Specifically, for each distance, we define three distinct SNR scenarios arranged from high to low. The network is trained with input data of varying SNRs, progressively transitioning from high to low every 10 epochs. When data of all SNRs are traversed, samples with random SNR are generated and fed to the network for the convergence of the network.

Training Parameters. We choose K in Eq. 4 as 4 and M in Eq. 7 as 1000. The number of restormer blocks in the network is set to [4, 6, 6, 8]. We train the network for 200 epochs using the ADAM optimizer [39] with a batch size of 20. The learning rate is initialized at 0.01 and decays by a factor of 0.7 every 10 epochs. The loss balance coefficients γ_1 and γ_2 are empirically set to $5e-4$ and $5e-2$ initially, and are updated to $5e-5$ and 1 after 40 epochs. γ_3 is always set to 5. Xavier initialization is used for the learnable coding functions. All experiments are conducted on the PyTorch platform [40], using an NVIDIA GeForce RTX 4090 GPU.

4.2 Comparison with the State-of-the-art Methods

To demonstrate the superiority of our method, we conduct a detailed comparison with traditional iToF approaches, including single frequency modulation and dual frequency modulation. The scenarios encompass multiple distance ranges (0-3 m, 30-33 m, 60-63 m, and 90-93 m) combined with varying SNRs, specifically high ($H_{snr} = 5.23$ dB), medium ($M_{snr} = 3.68$ dB) and low ($L_{snr} = 2.22$ dB). As shown in Fig. 5, we first compare our method with FisherToF [10] under single frequency modulation. While FisherToF achieves precise depth reconstruction at close range, it still suffers from the rapid decline in imaging quality over distance. We then compare our method with a variety of dual frequency modulation approaches, including sinusoid and square coding functions with Phase Shift

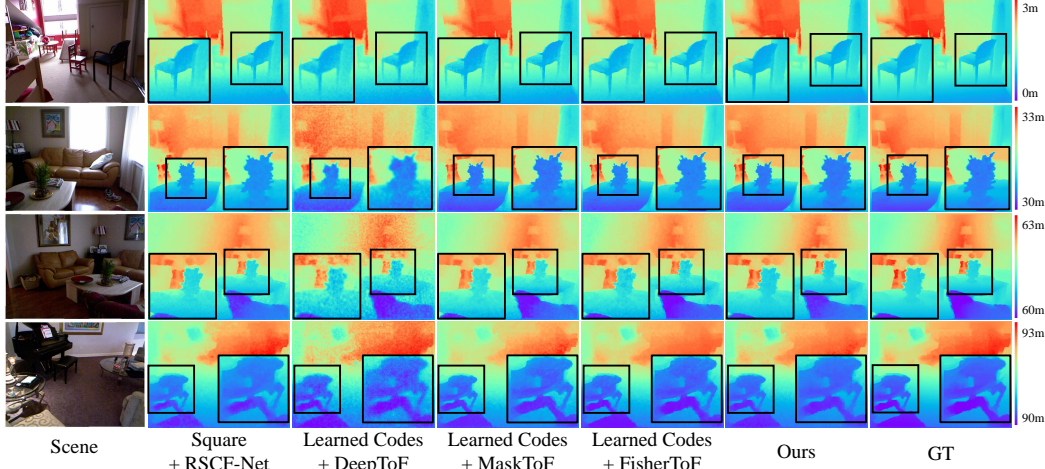


Figure 6: Comparisons with different coding scheme and reconstruction networks.

(PS) algorithm [5] and the learning-based DeepToF [21] method. Our method achieves the best performance across various distances and SNRs, using only single frequency modulation. We present a detailed comparison in Tab. 1 (a), with Mean Absolute Error (MAE) as the evaluation criterion.

We further substantiate the superiority of our method through an analysis of the learnable coding function and the proposed RSCF-Net. As for the coding function, considering the practical hardware implementability, we compare our learning coding functions with the square encoding functions with the same RSCF-Net. The quantitative results presented in Tab. 1 (b) prove that our learning encoding functions provides superior depth reconstruction and enhanced robustness to noise. Additionally, we perform a thorough comparison of our RSCF-Net with existing depth reconstruction networks with the same learned coding functions, including DeepToF [21], MaskToF [28] and FisherToF [10]. The quantitative results in Tab. 1 (c) confirm the effectiveness of our network. Fig. 6 presents the visual results of different methods across four distances under low SNR conditions, intuitively demonstrating the advantages of our approach.

4.3 Ablation Study

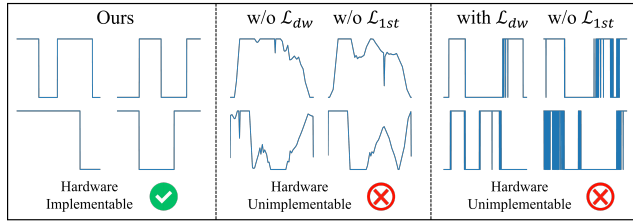


Figure 7: Visual ablations on \mathcal{L}_{dw} and \mathcal{L}_{1st} .

Table 2: Quantitative ablations with MAE(mm) as the evaluation metric.

Distance(m)	0-3	30-33	60-63	90-93
w/o \mathcal{L}_{fisher}	15.36	19.41	27.02	37.45
w/o CFEB	58.69	73.64	78.56	86.94
w/o MFFB	9.8	15.77	23.36	28.40
w/o ECA	10.22	13.01	21.41	26.06
Ours	8.52	12.86	18.20	23.51

We first conduct ablation experiments on the proposed double well function loss and first-order difference loss. Since the learned coding functions are primarily used to control the camera’s exposure, the absence of \mathcal{L}_{dw} and \mathcal{L}_{1st} results in coding functions that are entirely impractical to implement in hardware, which can be clearly illustrated in Fig. 7. In the next, we present a quantitative analysis in Tab. 2 to evaluate the impact of the fisher guidance loss and different network blocks. The values in Tab. 2 represent the average MAE measured under different SNRs at the same distance. The experimental results demonstrate the effectiveness of the introduced Fisher loss in guiding the network to learn an optimal coding functions. The ablation studies on different network blocks further validate the significant improvement in reconstruction quality brought by the proposed CFEB and MFFB.

5 Physical Experiment Results

Hardware Prototype. We develop a prototype system to validate the effectiveness of the proposed BE-ToF method in real-world scenarios. As illustrated in Fig. 8(a), the proposed system primarily comprises a cost-efficient fiber-based pulsed laser and an encodable image intensifier camera. The laser operates at a wavelength of 905 nm, with a pulse width of 20 ns and an average output power of 100 mW. It features a numerical aperture (NA) of 0.22, enabling wide-area illumination suitable for array-based depth imaging. A diffuser is placed at the laser output to ensure uniform illumination across the scene. The image intensifier camera is composed of a primary lens (75 mm, KOWA), image intensifier tubes, and a CCD sensor (ASI294MC), allowing for the detection of weak optical signals. To suppress ambient light interference, a 905 nm band-pass filter (FWHM ± 10 nm) is mounted in front of the lens. Both the laser and the image intensifier camera are driven in a 200 kHz burst mode using a function generator (DG4202, Rigol), with synchronization handled by a second generator. The demodulation function is configured with a 50 ns period, with the time delay flexibly adjustable via the function generator.

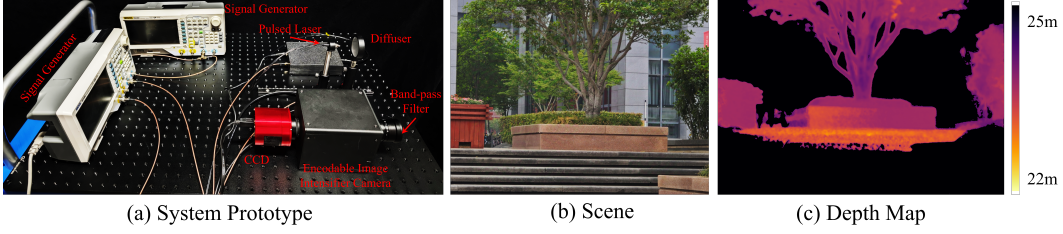


Figure 8: (a) System prototype of the BE-ToF, (b) Outdoor Scene, (c) Depth map.

Experimental Results. In the real-world experiment, we selected a highly challenging scene located approximately 23 meters away, featuring complex vegetation, surfaces with varying reflectivity, and significant ambient light interference. The resulting depth map is presented in Fig. 8(c), where the depths of objects such as steps, flower beds, and trees are clearly distinguishable. Notably, our system is also capable of reconstructing the continuous depth profile of marble surfaces. It is important to note that the BE-ToF system captures depth within a limited range in a single measurement. However, this constraint can be advantageous, as it effectively filters out background clutter and enables the system to concentrate on the depth region of interest. As illustrated in Fig. 8(c), both foreground and background elements are successfully suppressed, allowing for a clear focus on the target range.

6 Conclusion, Limitations, and Broader Impact

In conclusion, we propose a novel ToF imaging paradigm, termed BE-ToF. The BE-ToF system enables long-distance high-fidelity depth imaging by modulating and demodulating pulsed signals in burst mode using only single-frequency modulation. Additionally, we introduce a learnable end-to-end framework that jointly optimizes binarized coding functions and the reconstruction network to effectively handle varying SNRs across different distances, achieving state-of-the-art performance.

Limitations. Despite achieving both long-distance and high-fidelity depth imaging, our BE-ToF system is subject to limitations in its imaging range. As shown in Fig. 1, the operational range is confined between $\frac{c \cdot \tau}{2}$ and $\frac{c \cdot (\tau + T_m)}{2}$, with higher precision resulting in a narrower imaging range.

Broader Impact. The proposed BE-ToF system demonstrates strong potential for applications such as autonomous driving and topographic surveying, offering enhanced reconstruction quality and improved processing efficiency. However, its ability to perform long-distance depth imaging raises potential privacy concerns, particularly in scenarios where individuals may be unknowingly captured. Addressing these concerns responsibly is essential for real-world deployment.

References

- [1] Ruixuan Chen, Haowen Shu, Bitao Shen, Lin Chang, Weiqiang Xie, Wenchao Liao, Zihan Tao, John E Bowers, and Xingjun Wang. Breaking the temporal and frequency congestion of lidar by parallel chaos. *Nature Photonics*, 17(4):306–314, 2023.
- [2] Ricardo Roriz, Jorge Cabral, and Tiago Gomes. Automotive lidar technology: A survey. *IEEE Transactions on Intelligent Transportation Systems*, 23(7):6282–6297, 2021.
- [3] Simone Zennaro, Matteo Munaro, Simone Milani, Pietro Zanuttigh, Andrea Bernardi, Stefano Ghidoni, and Emanuele Menegatti. Performance evaluation of the 1st and 2nd generation kinect for multimedia applications. In *IEEE International Conference on Multimedia and Expo*, pages 1–6. IEEE, 2015.
- [4] David T Delpy, Mark Cope, Pieter van der Zee, Simon Arridge, Susan Wray, and JS Wyatt. Estimation of optical pathlength through tissue from direct time of flight measurement. *Physics in Medicine & Biology*, 33(12):1433, 1988.
- [5] Miles Hansard, Seungkyu Lee, Ouk Choi, and Radu Patrice Horaud. *Time-of-flight cameras: principles, methods and applications*. Springer Science & Business Media, 2012.
- [6] Larry Li et al. Time-of-flight camera—an introduction. *Technical White Paper*, (SLOA190B), 2014.
- [7] Mario Frank, Matthias Plaue, Holger Rapp, Ullrich Köthe, Bernd Jähne, and Fred A Hamprecht. Theoretical and experimental error analysis of continuous-wave time-of-flight range cameras. *Optical Engineering*, 48(1):013602–013602, 2009.
- [8] Yu Meng, Zhou Xue, Xu Chang, Xuemei Hu, and Tao Yue. itof-flow-based high frame rate depth imaging. In *Proceedings of the IEEE Conference on Computer Vision and Pattern Recognition*, pages 4929–4938, 2024.
- [9] Radu Horaud, Miles Hansard, Georgios Evangelidis, and Clément Ménier. An overview of depth cameras and range scanners based on time-of-flight technologies. *Machine vision and applications*, 27(7):1005–1020, 2016.
- [10] Jiaqu Li, Tao Yue, Sijie Zhao, and Xuemei Hu. Fisher information guidance for learned time-of-flight imaging. In *Proceedings of the IEEE Conference on Computer Vision and Pattern Recognition*, pages 16334–16343, 2022.
- [11] Stephane Poujouly and Bernard Journet. A twofold modulation frequency laser range finder. *Journal of Optics A: Pure and Applied Optics*, 4(6):S356, 2002.
- [12] Adrian PP Jongenelen, Donald G Bailey, Andrew D Payne, Adrian A Dorrington, and Dale A Carnegie. Analysis of errors in tof range imaging with dual-frequency modulation. *IEEE Transactions on Instrumentation and Measurement*, 60(5):1861–1868, 2011.
- [13] Ryan Crabb and Roberto Manduchi. Fast single-frequency time-of-flight range imaging. In *Proceedings of the IEEE Conference on Computer Vision and Pattern Recognition Workshops*, pages 58–65, 2015.
- [14] Aongus McCarthy, Gregor G Taylor, Jorge Garcia-Armenta, Boris Korzh, Dmitry V Morozov, Andrew D Beyer, Ryan M Briggs, Jason P Allmaras, Bruce Bumble, Marco Colangelo, et al. High-resolution long-distance depth imaging lidar with ultra-low timing jitter superconducting nanowire single-photon detectors. *Optica*, 12(2):168–177, 2025.
- [15] Mamadou Diop and Keith St. Lawrence. Improving the depth sensitivity of time-resolved measurements by extracting the distribution of times-of-flight. *Biomedical Optics Express*, 4(3):447–459, 2013.
- [16] Shinzo Koyama, Motonori Ishii, Shigeru Saito, Masato Takemoto, Yugo Nose, Akito Inoue, Yusuke Sakata, Yuki Sugiura, Manabu Usuda, Tatsuya Kabe, et al. A 220 m-range direct time-of-flight 688 × 384 cmos image sensor with sub-photon signal extraction (spse) pixels using vertical avalanche photo-diodes and 6 khz light pulse counters. In *2018 IEEE Symposium on VLSI Circuits*, pages 71–72. IEEE, 2018.
- [17] Matteo Perenzoni, Daniele Perenzoni, and David Stoppa. A 64 × 64-pixels digital silicon photomultiplier direct tof sensor with 100-mphotons/s/pixel background rejection and imaging/altimeter mode with 0.14% precision up to 6 km for spacecraft navigation and landing. *IEEE Journal of Solid-State Circuits*, 52(1):151–160, 2016.
- [18] Tang Xu, Qianyu Chen, Dajing Bian, and Yue Xu. A near-infrared single-photon detector for direct time-of-flight measurement using time-to-amplitude-digital hybrid conversion method. *IEEE Transactions on Instrumentation and Measurement*, 73:1–9, 2023.

- [19] David Droeschel, Dirk Holz, and Sven Behnke. Multi-frequency phase unwrapping for time-of-flight cameras. In *IEEE International Conference on Intelligent Robots and Systems*, pages 1463–1469. IEEE, 2010.
- [20] Dwi Hanto, Hari Pratomo, Agitta Rianaris, Andi Setiono, Sartika Sartika, Mohamad Syahadi, Eko Joni Pristianto, Dayat Kurniawan, Dwi Bayuwati, Hendra Adinanta, et al. Time of flight lidar employing dual-modulation frequencies switching for optimizing unambiguous range extension and high resolution. *IEEE Transactions on Instrumentation and Measurement*, 72:1–8, 2023.
- [21] Shuochen Su, Felix Heide, Gordon Wetzstein, and Wolfgang Heidrich. Deep end-to-end time-of-flight imaging. In *Proceedings of the IEEE Conference on Computer Vision and Pattern Recognition*, pages 6383–6392, 2018.
- [22] Christopher A Metzler, Hayato Ikoma, Yifan Peng, and Gordon Wetzstein. Deep optics for single-shot high-dynamic-range imaging. In *Proceedings of the IEEE Conference on Computer Vision and Pattern Recognition*, pages 1375–1385, 2020.
- [23] Qilin Sun, Ethan Tseng, Qiang Fu, Wolfgang Heidrich, and Felix Heide. Learning rank-1 diffractive optics for single-shot high dynamic range imaging. In *Proceedings of the IEEE Conference on Computer Vision and Pattern Recognition*, pages 1386–1396, 2020.
- [24] Shijie Nie, Lin Gu, Yinqiang Zheng, Antony Lam, Nobutaka Ono, and Imari Sato. Deeply learned filter response functions for hyperspectral reconstruction. In *Proceedings of the IEEE Conference on Computer Vision and Pattern Recognition*, pages 4767–4776, 2018.
- [25] Elias Nehme, Daniel Freedman, Racheli Gordon, Boris Ferdman, Lucien E Weiss, Onit Alalouf, Tal Naor, Reut Orange, Tomer Michaeli, and Yoav Shechtman. Deepstorm3d: dense 3d localization microscopy and psf design by deep learning. *Nature Methods*, 17(7):734–740, 2020.
- [26] Vincent Sitzmann, Steven Diamond, Yifan Peng, Xiong Dun, Stephen Boyd, Wolfgang Heidrich, Felix Heide, and Gordon Wetzstein. End-to-end optimization of optics and image processing for achromatic extended depth of field and super-resolution imaging. *ACM Transactions on Graphics*, 37(4):1–13, 2018.
- [27] Ziyi Guo, Jiaqu Li, Kanghui Wang, Tao Yue, and Xuemei Hu. End-to-end fluorescence lifetime imaging with optimized encoding and exposure allocation. In *IEEE International Conference on Computational Photography*, pages 1–12. IEEE, 2024.
- [28] Ilya Chugunov, Seung-Hwan Baek, Qiang Fu, Wolfgang Heidrich, and Felix Heide. Mask-tof: Learning microlens masks for flying pixel correction in time-of-flight imaging. In *Proceedings of the IEEE Conference on Computer Vision and Pattern Recognition*, pages 9116–9126, 2021.
- [29] Amit Agrawal and Yi Xu. Coded exposure deblurring: Optimized codes for psf estimation and invertibility. In *2009 IEEE Conference on Computer Vision and Pattern Recognition*, pages 2066–2073. IEEE, 2009.
- [30] Miao Liao, Liang Wang, Ruigang Yang, and Minglun Gong. Light fall-off stereo. In *Proceedings of the IEEE Conference on Computer Vision and Pattern Recognition*, pages 1–8. IEEE, 2007.
- [31] Syed Waqas Zamir, Aditya Arora, Salman Khan, Munawar Hayat, Fahad Shahbaz Khan, and Ming-Hsuan Yang. Restormer: Efficient transformer for high-resolution image restoration. In *Proceedings of the IEEE Conference on Computer Vision and Pattern Recognition*, pages 5728–5739, 2022.
- [32] Qilong Wang, Banggu Wu, Pengfei Zhu, Peihua Li, Wangmeng Zuo, and Qinghua Hu. Eca-net: Efficient channel attention for deep convolutional neural networks. In *Proceedings of the IEEE Conference on Computer Vision and Pattern Recognition*, pages 11534–11542, 2020.
- [33] V Jelic and F Marsiglio. The double-well potential in quantum mechanics: a simple, numerically exact formulation. *European Journal of Physics*, 33(6):1651, 2012.
- [34] Nathan Silberman, Derek Hoiem, Pushmeet Kohli, and Rob Fergus. Indoor segmentation and support inference from rgb-d images. In *Proceedings of the European Conference on Computer Vision*, pages 746–760. Springer, 2012.
- [35] Junho Jeon, Sunghyun Cho, Xin Tong, and Seungyong Lee. Intrinsic image decomposition using structure-texture separation and surface normals. In *Proceedings of the European Conference on Computer Vision*, pages 218–233. Springer, 2014.
- [36] Beomjun Kim, Jean Ponce, and Bumsu Ham. Deformable kernel networks for joint image filtering. *International Journal of Computer Vision*, 129(2):579–600, 2021.

- [37] Lingzhi He, Hongguang Zhu, Feng Li, Huihui Bai, Runmin Cong, Chunjie Zhang, Chunyu Lin, Meiqin Liu, and Yao Zhao. Towards fast and accurate real-world depth super-resolution: Benchmark dataset and baseline. In *Proceedings of the IEEE Conference on Computer Vision and Pattern Recognition*, pages 9229–9238, 2021.
- [38] Yoshua Bengio, Jérôme Louradour, Ronan Collobert, and Jason Weston. Curriculum learning. In *Proceedings of the International Conference on Machine Learning*, pages 41–48, 2009.
- [39] Diederik P Kingma and Jimmy Ba. Adam: A method for stochastic optimization. *arXiv preprint arXiv:1412.6980*, 2014.
- [40] Adam Paszke, Sam Gross, Soumith Chintala, Gregory Chanan, Edward Yang, Zachary DeVito, Zeming Lin, Alban Desmaison, Luca Antiga, and Adam Lerer. Automatic differentiation in pytorch. 2017.